Energy & Environmental Science

PAPER

View Article Online
View Journal | View Issue

Cite this: *Energy Environ. Sci.*, 2014, **7**, 2359

Large fill-factor bilayer iodine perovskite solar cells fabricated by a low-temperature solution-process

Qi Wang,† Yuchuan Shao,† Qingfeng Dong,† Zhengguo Xiao, Yongbo Yuan and Jinsong Huang*

Received 21st January 2014
Accepted 11th April 2014

DOI: 10.1039/c4ee00233d

www.rsc.org/ees

This work studied the influence of the methylammonium iodide/lead iodine precursor ratio on the perovskite film morphology and device performance. Using a non-stoichiometric precursor solution was demonstrated to be critical to form stoichiometric perovskite films. The compositions of the spun perovskite films were very sensitive to the surface of substrates, and can be very different from that in precursor solutions. Remarkably, we found that the unique double fullerene layers adopted could dramatically reduce dark current leakage by forming a Schottky junction with the anode, and effectively passivate traps in perovskite to increase the efficiency by boosting the fill factor to above 80% for perovskite solar cells.

Broader context

Harnessing solar energy has been acknowledged as a promising way to solve the world energy crisis. In past decades, solution process thin film photovoltaics have been intensively attractive in the quest for low cost, light weight and easily fabricated solar cells. Recently, organometal halide perovskites have been discovered as excellent absorbers for solar cells. Dye sensitized solar cells using this material have shot up to high efficiencies of ~15%. When it comes to planar thin film perovskite solar cells, it has been found to be very challenging to form high quality perovskite films by direct spin coating of the mixed lead iodine/methylammonium halide stoichiometric solution. We studied the influence of the stoichiometric precursor ratio of the lead iodine/methylammonium halide solution on the perovskite film morphology as well as the device performance. A non-stoichiometric precursor ratio was found to be more suitable for perovskite formation to achieve a higher efficiency. Moreover, a unique double fullerene structure was applied and could be demonstrated as one of the reasons for achieving the record high fill factor of 80% in perovskite solar cells.

1. Introduction

Solution processed low cost, high efficiency photovoltaic devices have been persistently pursued over the past decade for renewable solar to electric energy conversion.[1–6] Recently, organolead halide perovskites have arisen as excellent earth abundant photovoltaic materials to compete with organic semiconductors[3,7] and quantum dots[6] due to their small bandgap, strong absorption, excellent crystallinity and long charge diffusion length.[4,8–21] They have been applied as an active layer in both mesoporous structure and planar heterojunction (PHJ) solar cells with the highest demonstrated power conversion efficiency (PCE) exceeding 15%.[4,8–15] It has been recently revealed that halide perovskites have superior charge diffusion length to most solution-processed organic photovoltaic (OPV) and quantum-dot photovoltaic (QDPV) materials.[4,11,15] The balanced electron–hole diffusion lengths were found to approach the optical absorption length in solution-processed methylammonium lead iodide ($CH_3NH_3PbI_3$) and are ten times longer than the optical absorption length in solution-processed $CH_3NH_3PbI_{3-x}Cl_x$.[4,11,15] To date, perovskite films have been formed by versatile film deposition approaches such as spin-coating,[8,13,14] sequential deposition of the inorganic and organic precursor[9] and co-evaporation of the precursors.[10] While low temperature spin-coating is among the simplest methods to fabricate low-cost solar cell devices, it was found to be very challenging to form continuous perovskite films by spin-coating the directly mixed lead iodine (PbI_2) and methylammonium halide blend precursor solution.[2,7,17,18,20] Non-fully covered perovskite films were frequently observed which might ascribe to the interaction of perovskite with the substrate surface.[17,18] We observed very rough perovskite films with microfiber formation on perovskite films as shown in Fig. 1a using the stoichiometry precursor solutions (a molar ratio of PbI_2 : methylammonium iodide (CH_3NH_3I) = 1 : 1), leading to a large device leakage current as well as low fill factor (FF) and small open circuit voltage (V_{OC}) (Fig. S1†).

In this manuscript, we report a low-temperature solution process to form a relatively continuous $CH_3NH_3PbI_3$ layer. It was found that the perovskite morphology is sensitive to precursor's composition variation and a non-stoichiometry precursor ratio

Department of Mechanical and Materials Engineering, Nebraska Center for Materials and Nanoscience, University of Nebraska-Lincoln, Lincoln, Nebraska 68588-0656, USA. E-mail: jhuang2@unl.edu

† Q.W., Y. S. and Q. D. contributed to this work equally.

could lead to a high device efficiency of 12.2%. The application of a spun conformal fullerene layer was found critical in avoiding leakage by covering the perovskite films and the exposed anode area. Using a unique double fullerene layer structure to passivate the trap states, devices with a record FF of 80.1% were achieved for perovskite solar cells under one sun illumination.

2. Experimental

CH_3NH_3I was synthesized using the method described by Michael M. Lee, *et al.*[8] A concentrated aqueous solution of hydroiodic acid (HI) (15.0 ml, 57 wt% in water, Alfa Aesar) was reacted with methylamine (CH_3NH_2) (13.5 ml, 40 wt% in aqueous solution, Alfa Aesar) at 0 °C for 2 h with constant stirring under a nitrogen atmosphere. Methylammonium iodide was crystallized through removing the solvent by a rotary evaporator. The generated white powder was washed with diethyl ether (Alfa Aesar) three times and dried under vacuum overnight.

The indium tin oxide (ITO) substrates were cleaned and the poly(3,4-ethylenedioxythiophene) poly(styrenesulphonate) (PEDOT:PSS) layer was spun on ITO as routine.[1] CH_3NH_3I and PbI_2 precursors were dissolved in anhydrous *N*,*N*-dimethylformamide (DMF) at different concentrations from 150 mg ml^{-1} to 350 mg ml^{-1}, and mixed at different ratios. The mixture solutions were spun onto PEDOT:PSS at a rate of 4000 rounds per minute for 30 seconds. The perovskite films were annealed at 100 °C for 15–60 minutes. Here, the combination of a high precursor solution concentration and a high spin rate was used to reduce the roughness of the perovskite films. After the spin-coating of perovskite films, 30 nm C_{60} was thermal-evaporated with a deposition rate of 2–3 Å s^{-1}. The [6,6]-phenyl-C_{61}-butyric acid methyl ester (PCBM) and indene-C_{60} bisadduct (ICBA) were dissolved in dichlorine benzine (DCB) at a concentration of 20–30 mg ml^{-1} and were spun on the perovskite layer for some devices, which was followed by the low temperature annealing at 100 °C for 10–60 minutes. The highest efficiency devices have perovskite annealed at 100 °C for 60 minutes before ICBA coating, and 100 °C for 30 minutes after ICBA coating. The devices were finished by the evaporation of a 7 nm 2,9-dimethyl-4,7-diphenyl-1,10-phenanthroline (BCP) and 100 nm aluminum electrode. The active device area (defined by the overlapping of ITO and aluminum electrode) is 0.06 cm^2.

Absorption spectra, photoluminescence (PL) spectra, scanning electron microscopy (SEM) pictures and X-ray diffraction (XRD) patterns of the films were recorded by using an Evolution 201 UV-Visible Spectrophotometer, iHR320 Photoluminescence Spectrometer, Quanta 200 FEG Environmental Scanning Electron Microscope, and Rigaku D/Max-B X-ray diffractometer with Bragg-Brentano parafocusing geometry, respectively. It should be noted that the perovskite films for XRD measurement were spun on PEDOT:PSS coated silicon substrates, giving the same compositions with real devices. The photocurrents of the devices were measured under AM1.5G irradiation (100 mW cm^{-2}) with a xenon-lamp based solar simulator (Oriel 67005, 150 W Solar Simulator). A Schott visible-colour glass-filtered (KG5 colour-filtered) Si diode (Hamamatsu S1133) was used to calibrate the light intensity before photocurrent measurement.

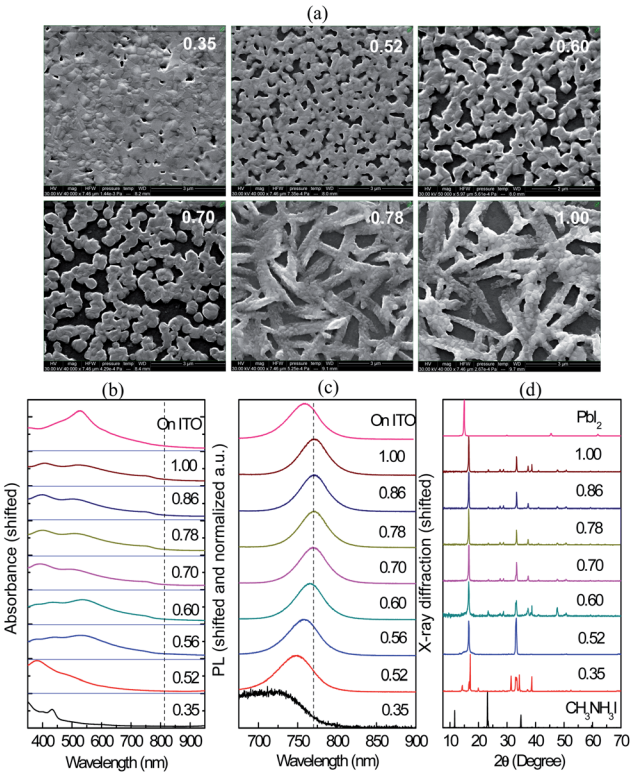

Fig. 1 Top view SEM images (a), absorption spectra (b), PL spectra (c) and XRD patterns (d) of the iodine perovskite films spun from solutions with a precursor ratio from 0.35 to 1. All the perovskite films in (b) and (c) were spun on PEDOT:PSS except the ones that are labeled as on ITO. The precursor ratio of the perovskite films spun on ITO is 0.7. The scale bars of SEM images are 2 μm in the sample with a precursor ratio of 0.6 and 3 μm for all others. The absorbance spectra are shifted by 2 with respect to each other, and the PL spectra are normalized and shifted with respective to each precursor composition for clarity. The vertical dashed lines in the absorption spectra and PL spectra, which show the reported absorption band edge and PL peak of iodine perovskite respectively, are added as guidance to the eye.

3. Results and discussion

Our method of varying the precursor ratio in solution stems from the observation that two perovskite films formed on different surfaces are strikingly different in absorption and PL spectra, as shown in Fig. 1b and c. These two films were spun on ITO and PEDOT:PSS from the same solution with a PbI_2/CH_3NH_3I precursor molar ratio (defined as the precursor ratio) of 0.7. It was speculated that the difference origins from the different affinities of the organic and inorganic precursors to the different surfaces. To verify that we varied the precursor ratio from 0.35 to 1.0 to study the formation of perovskite on PEDOT:PSS which is the hole extraction layer in our devices. The absorption, PL, and XRD patterns are shown in Fig. 1b–d as well to evaluate the formation of stoichiometric perovskite films. As shown in Fig. 1b, the films with a small amount of PbI_2 have a strong absorption peak in the UV range. The increased PbI_2 percentage in the precursor solution causes slightly red-shifted peak and enhanced absorption. Upon an increased

precursor ratio to 0.6, there is a distinct transition of absorption spectra patterns from strong absorption in the UV-blue range to a broad absorption across the UV-visible range which indicates the formation of perovskite. The transition of absorption patterns with an increased precursor ratio from 0.52 to 0.6 is associated with a PL peak shift from 750 nm to 765 nm, as shown in Fig. 1c. When the precursor ratio is over 0.70, the PL peak is fixed at 770 nm which is close to that of the previously reported stoichiometry perovskite.[9] Further increasing the PbI_2 ratio over 0.7 does not change the absorption and PL spectrum shape or the peak intensity. The PL and absorption peaks of the film spun on ITO with the precursor ratio of 0.7 are close to those of the films on PEDOT:PSS with the precursor ratio of 0.56, indicating more PbI_2 content in the film spun on PEDOT:PSS. It might ascribe to the better affinity of PbI_2 to the amphiphilic PEDOT:PSS than that to ITO. XRD patterns in Fig. 1d reveal tetragonal perovskite forms with a small amount of PbI_2 added in the precursor solution, while impurity peaks disappear when the precursor ratio is over 0.6.[22] The non-unit precursor ratio for stoichiometric perovskite film formation indicates that the composition of the spun films is different from that in the precursor solution, which should attribute to the different affinities of CH_3NH_3I and PbI_2 to the substrates. The top surface SEM images of perovskite films with different precursor ratios are shown in Fig. 1a. Increasing the amount of PbI_2 in the films generally increases the film roughness, and a lot of microfibers are observed when the precursor ratio is larger than 0.8. The tiled cross-section and top-view SEM image of a perovskite film with a precursor ratio of 0.78 (Fig. 2a) showed distinct two-layer structures in the formed perovskite films: a flat, continuous bottom layer and a discontinuous top layer with many microstructures. The microstructures of the top layer vary dramatically with precursor ratios as shown in Fig. 1a. It is not yet clear why such two-layer structures form but it is certainly related to the spin-coating process because the feature of the microstructures varies with different spin-coating parameters.

The typical structure used to evaluate the formed perovskite films is shown in Fig. 2b which is similar to the PHJ OPVs.[23] It is noted that a perforation in the perovskite film is sketched for better illustration of the working mechanism of our devices in the follow-up discussion. It does not indicate that the perovskite film is totally discontinous because the size of the hole is enlarged for clarity. A double layer fullerene, with a spun PCBM or ICBA layer underneath followed by a thermal evaporated C_{60} layer, was used as the electron extraction layer. BCP is a well-known electron transport/hole blocking layer which has been widely used in organic light emitting diodes, organic photodetectors and organic photovoltaic devices.[24–28] Its functions have been thoroughly studied in OPVs including (1) blocking holes because of the poor hole mobility; (2) transporting electrons with large electron mobility; (3) reducing the damage of the fullerene layer followed by metal deposition. To optimize the device performance, the composition and thickness of the $CH_3NH_3PbI_3$ films were tuned by varying the ratio and concentration of the precursor solutions, and different fullerene electron extraction layers were applied. Fig. 3a shows composition dependent photocurrent curves for the devices fabricated by the same procedure except to the precursor ratio. In the devices with increased PbI_2 percentage, the more perovskite formed gives a larger short circuit current density (J_{SC}) due to the increased absorption, while the V_{OC} of the devices declines slightly. The films spun from solutions with a precursor ratio larger than 0.8 often yielded non-working devices due to the large leakage current. This agrees with the morphological study by SEM (Fig. 1a) that more PbI_2 in the films generally increase the roughness with a lot of microfibers showing up on the surface, possibly due to the crystallization of perovskite and/or PbI_2. The devices with a precursor molar ratio of 0.6–0.7 have the largest PCE. This observation provides a plausible explanation for the previously reported low efficiency PHJ perovskite solar cells by the solution process.

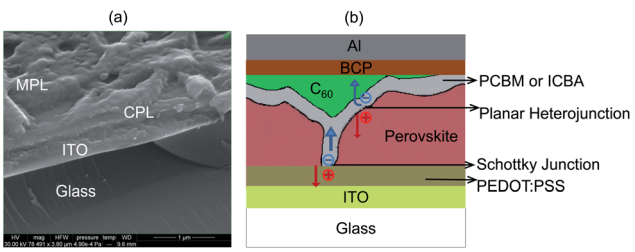

Fig. 2 (a) Tilted cross-section SEM image of a perovskite film spun from solution with a precursor ratio of 0.78. The continuous perovskite layer (CPL) and the microstructure perovskite layer (MPL) are labeled. The scale bar is 1 μm; (b) the schematic device structure of the perovskite PV devices. An ICBA or PCBM layer was sketched as a conformal layer and the two types of junction were also depicted. The thickness of the each layer was not in scale with the real thickness for clarity.

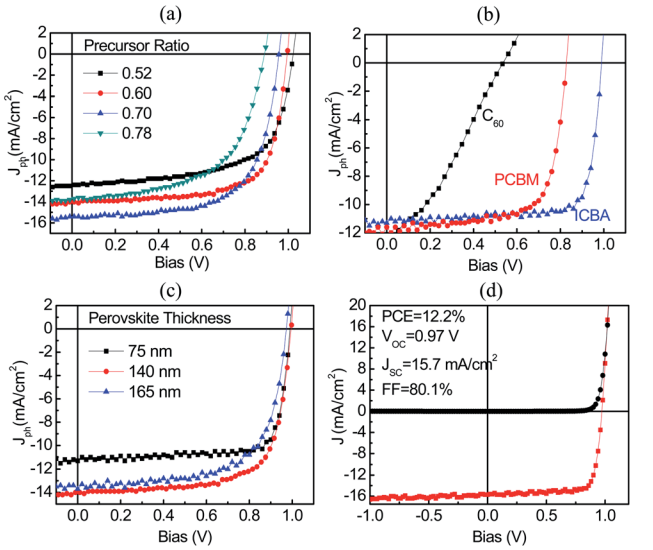

Fig. 3 The photocurrents of the devices under AM 1.5 simulated illumination with different precursor ratios (a), different acceptor layers (b), and different thicknesses (c). The devices in (a) have a thickness of 140 nm and an ICBA acceptor layer; the devices in (b) have a precursor ratio of 0.6 and a thickness of 75 nm. The devices in (c) have a precursor ratio of 0.6 and an ICBA acceptor layer. (d) The photo- and dark-currents of the highest efficiency device.

Table 1 Performance of devices with different precursor molar ratios, perovskite thicknesses and fullerene derivative layers

Device structure	Perovskite thickness	Precursor molar ratio	J_{SC} (mA cm^{-2})	V_{OC} (V)	FF (%)	PCE (%)
ITO/PEDOT:PSS/perovskite/	75 nm	0.60	12.4	0.82	74.1	7.53
PCBM/C_{60}/BCP/AL		0.70	11.2	0.86	73.7	7.10
		0.78	10.4	0.87	74.7	6.76
		0.86	9.97	0.88	74.1	6.50
	100 nm	0.60	11.9	0.91	67.2	7.28
		0.70	14.2	0.86	60.4	7.38
		0.78	12.7	0.89	67.6	7.64
		0.86	14.5	0.89	71.4	9.22
	140 nm	0.52	13.5	0.9	64.9	7.89
		0.60	15.3	0.86	57.3	7.54
		0.78	15.9	0.88	72.2	10.1
		0.86	16.3	0.8	60.8	7.93
ITO/PEDOT:PSS/perovskite/	75 nm	0.60	11.3	0.98	80.0	8.83
ICBA/C_{60}/BCP/AL	140 nm	0.52	12.5	1.02	63.8	8.14
		0.60	14.0	0.99	71.1	9.85
		0.60	15.7	0.97	80.1	12.2
		0.70	15.4	0.96	65.3	9.66
		0.78	13.8	0.88	58.9	7.15
	165 nm	0.43	7.05	1.06	47.5	3.55
		0.52	9.13	1.05	55.8	5.35
		0.60	13.7	0.98	64.4	8.65
		0.70	15.3	0.94	46.6	6.70
		0.78	14.1	0.93	68.4	8.97
ITO/PEDOT:PSS/perovskite/C_{60}/BCP/AL	75 nm	0.60	12.2	0.53	33.1	2.14

Fig. 3b illustrates the photocurrent of devices with different spun fullerene or fullerene derivatives. It is found that the application of spun PCBM and ICBA significantly increases the V_{OC} of the perovskite photovoltaic devices. The device fabrication parameters of the three devices studied here were controlled to be the same except for the fullerene layers. The V_{OC} of the devices with perovskite coated by ICBA reaches 1.06 V which is 0.1–0.2 V larger than that of the device with PCBM interfacial modification, as shown in Table 1. The V_{OC} enhancement in the devices with spun PCBM or ICBA can be explained by the Schottky junction formed between the spun fullerene films and the underneath PEDOT:PSS layer which is described below.

A film thickness close to the charge diffusion length in the perovskite films is needed for strong absorption of light in the red spectral range. The thicknesses of the devices with different precursor ratios were optimized, and the results are summarized in Table 1. A typical thickness dependent photocurrent of the devices with a non-optimized annealing time of 15 minutes is shown in Fig. 3c. The J_{SC} increases with the film thickness until a maximum of 14.0 mA cm^{-2} is reached at the optimized perovskite thickness of 140 nm, and then reduces with the increased film thickness. Further increasing the film thickness to enhance the J_{SC} is likely hindered by the charge diffusion length in iodine perovskite which was reported to be around 100 nm.[11,15] The optimized precursor ratio increases from 0.60 to 0.78 with increased thickness of the perovskite layer, which can be explained by the decreased affinity of PbI_2 to PEDOT:PSS for the material far away from the PEDOT:PSS surface. A larger percentage of PbI_2 in precursor solution is needed in the thick films to satisfy the stoichiometric composition. The film-thickness dependent V_{OC} variation behavior is different in devices with different fullerene layers. The V_{OC} remains almost invariant in the device with an ICBA acceptor layer, while increases in the device with a PCBM acceptor layer (Fig. S2†), which might be ascribed to the observed lower dark current in the thicker film devices.

The FFs of the perovskite devices are sensitive to the composition and thickness of the perovskite layer as well as the electron extraction layers. The FF variation with the precursor ratio exhibits a peak value in the molar ratio of 0.6, as shown in Table 1. A thinner perovskite layer also gives a larger FF, most likely due to more efficient collection of charges and reduced recombination in the thinner perovskite films. The FFs are also comparable for the devices with PCBM and ICBA electron extraction layers, while a slightly larger FF of 80.1% is observed in the device with ICBA layers. This is in striking contrast to OPVs in which ICBA always yields a smaller FF than PCBM. To the best of our knowledge, the obtained FF is the highest among all the perovskite solar cells reported. The large FF and V_{OC} in our bilayer structure devices with an ICBA layer indicate that the charge recombination limiting the efficiency in perovskite solar cells is different from that in OPVs or QDPVs.

The optimized devices have a precursor ratio of 0.6, a thickness of 140 nm, and an ICBA acceptor layer. The thermal annealing time of the perovskite film was optimized to 60 minutes under 100 °C. Meanwhile, perovskite/ICBA layers were annealed 30 minutes at the same temperature. The highest efficiency device with photo- and dark-currents shown in Fig. 3d has a J_{SC} of 15.7 mA cm^{-2}, a V_{OC} of 0.97 V, a FF of 80.1% and a

PCE of 12.2%. It is expected that the slight annealing after ICBA coating drives the diffusion of ICBA into the perovskite for a larger contact area. The performance of our high efficiency device did not show reduction when it was tested with a mask to define the device area and avoid light piping (Fig. S3†). No obvious hysteresis of photocurrent was observed by changing the voltage sweep rates or direction (Fig. S4†).

It is noted that a very similar device structure was reported previously which also uses a PCBM or an ICBA electron transport layer. Their reported V_{OC} of the device with a C_{60} electron collection layer is comparable to what we have, but the V_{OC} of the PCBM or ICBA only devices are 0.3 to 0.4 V smaller than what were achieved in this work. And the FF reported here is much larger than that previously reported. The huge improvement of device performance in this work can be explained by the unique double fullerene layer introduced in addition to a better controlling of active layer composition by varying the precursor ratio. The first rewarding aspect for applying this double fullerene layer structure is the spun fullerene layer that can effectively eliminate device leakage. As mentioned above, rough perovskite top surfaces are generally observed in the SEM images, and devices fabricated by these films often exhibit a large leakage current. It is therefore speculated that there is still an exposed PEDOT:PSS area which is not fully covered by perovskite. The spun fullerene layer must cover the exposed PEDOT:PSS area by forming a conformal layer, which is evidenced by the SEM image of the perovskite film covered by a spun ICBA layer as shown in Fig. 4a–c. This conformal fullerene covering effectively eliminates the leakage current. To verify this speculation, we made devices with or without a solution processed fullerene layer:

Device I: ITO/PEDOT:PSS/perovskite (140 nm)/C_{60} (50 nm, thermal-evaporated)/BCP/Al.

Device II: ITO/PEDOT:PSS/perovskite (140 nm)/C_{60} (20 nm, spun)/C_{60} (30 nm, thermal evaporation)/BCP/Al.

Fig. 4d shows the dark current curves of the devices with and without a spun C_{60} layer. The device without a spun C_{60} layer exhibits a huge leakage current density larger than 10 mA cm^{-2} even under a small reverse bias of 0.1 V. Nevertheless, after inserting a spun C_{60} layer onto the perovskite, the dark current is dramatically reduced by 3–4 orders of magnitude, demonstrating that a spun fullerene layer is crucial in preventing leakage. In order to find out whether the solvent of fullerene played a role in reducing leakage, we also made devices with DCB washed perovskites. No obvious morphological change of the perovskite film surface was observed in SEM images before and after DCB washing (Fig. 4a and S5†). Meanwhile, the dark current of the devices fabricated by DCB washed perovskite films still shows large leakage, although it was reduced several times (Fig. 4d). As the DCB wash effect, though exists, is relatively minor, we then explained that the spun fullerene forms a conformal layer that cover most of the perovskite surface to prevent leakage.

The contact of fullerenes with PEDOT:PSS forms a Schottky junction, which was discovered by us previously.[29] Consequently, our devices consist of two types of devices, perovskite/fullerene PHJ devices and PEDOT:PSS/fullerene Schottky junction devices, connected in parallel. This scenario is sketched in the device structure shown in Fig. 2b. The overall V_{OC} is determined by both perovskite cell and the Schottky junction cell based on their relative cell area. The contact of PCBM and ICBA with PEDOT:PSS should not compromise the V_{OC} of the whole devices because a large V_{OC} of around 0.87 V and 0.95 V can be obtained from the PCBM/PEDOT:PSS and ICBA/PEDOT:PSS Schottky junction devices.[29] However, if C_{60} is spun onto perovskite, the device overall V_{OC} was reduced to ~0.5 V because the V_{OC} of a C_{60}/PEDOT:PSS Schottky junction is only around 0.45 V.[29]

The other important role that this double fullerene layer structure plays is its better passivation effect of traps in perovskite. To verify this scenario, we conducted thermal admittance spectroscopy (TAS) to quantitatively analyze the passivation of perovskite by PCBM and C_{60}.[30] TAS is a well-established technique for determination of the defect density of states which has been broadly applied in understanding defects in the thin film solar cells and organic solar cells.[31,32] The trap density of states (tDOS) distribution can be derived from the angle frequency dependent capacitance *via*,

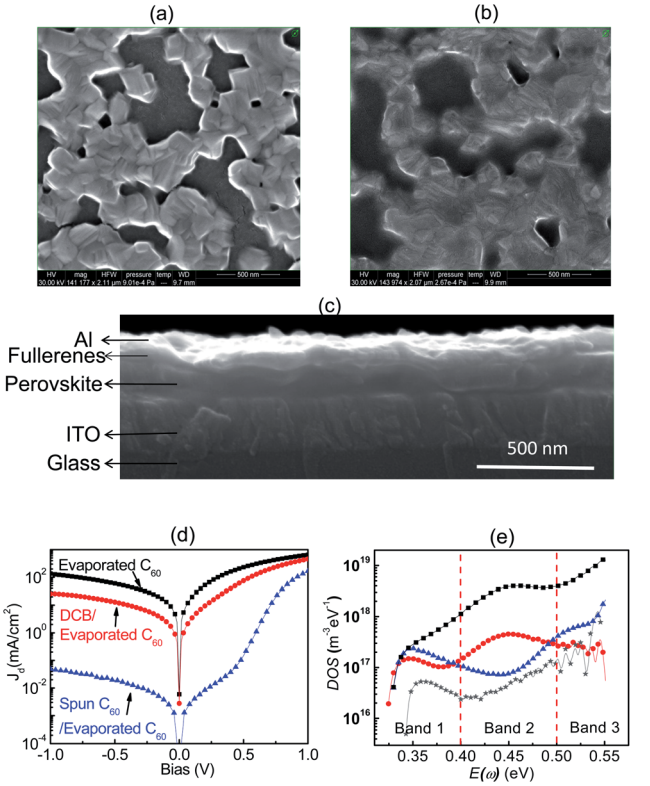

Fig. 4 (a) Top view of the SEM image of the as-spun perovskite film. (b) Top view SEM image of the perovskite film after ICBA spin-coating. The perovskite films in (a) and (b) were spun from the solution with a precursor ratio of 0.6 and a concentration of 250 mg ml^{-1}. The scale bar is 500 nm. (c) Cross-section SEM of a working device with a thin (75 nm) perovskite layer. (d) Dark current of perovskite devices with different fullerene layer fabrication processes. Black square, red circle, blue triangle curves are for the devices with a 50 nm C_{60}, perovskite film washed by the DCB solvent, 20 nm spun C_{60} plus 30 nm evaporated C_{60}, respectively. (e) Trap density of states (tDOS) for devices passivated by single PCBM layer (blue triangles), single C_{60} layer (red dots), PCBM/C_{60} double fullerene layers (grey stars); black squares represent the devices without fullerene passivation.

$$N_T(E_\omega) = -\frac{V_{bi}}{qW}\frac{dC}{d\omega}\frac{\omega}{k_B T}$$

where V_{bi} is the built-in potential, q is the element charge, W is the depletion width, C is capacitance, ω is the applied angular frequency, k_B is the Boltzmann's constant, and T is the temperature. V_{bi} and W are extracted from the capacitance–voltage measurement. The applied angular frequency ω defines the energy demarcation,

$$E_\omega = k_B T \ln\left(\frac{\omega_0}{\omega}\right)$$

The trap states below the energy demarcation can capture or emit the charge with the given ω and contribute to the capacitance while the defect states above the energy demarcation cannot. Thus the frequency differential capacitance measurements provide the distribution of tDOS, which are performed using the E4980A Precision LCR Meter from Agilent at a frequency between 0.1 to 1000 kHz.

The results in Fig. 4e show that the devices without any fullerene layer have a relatively large trap density between 1×10^{17} and 1×10^{19} m^{-3} eV^{-1} (black squares) which is detrimental to the device performance. Three trap bands can be identified as labeled in the figure (separated by red dotted lines). After depositing the C_{60} or PCBM layer, the tDOS reduced dramatically, indicating that both the C_{60} and PCBM effectively passivated the defects in perovskite films. It is noticed that C_{60} and PCBM have different but complementary passivation capability to the different trap bands. PCBM prefers to passivate the trap states in band 2 (0.40–0.50 eV) and C_{60} has a stronger passivation effect on trap states with a trap depth larger than 0.50 eV (band 3). The tDOS of the device with PCBM and C_{60} double fullerene layers with an optimum thermal annealing time is smaller than those with either PCBM or C_{60}, and is about two orders of magnitude lower than the device without fullerenes in the whole defect spectral range. This result demonstrated that the PCBM and C_{60} cooperate with each other well and further reduce the trap densities. This explains the better device performance, especially the record FF, in our optimized devices with double fullerene layers.

4. Conclusion

In summary, we reported the 12.2% iodine perovskite solar cell devices fabricated by a low temperature solution process with a simple bilayer device structure. Our finding of substrate surface sensitive perovskite composition is critical in the design and fabrication of other solution processed perovskite photovoltaic devices, especially chlorine containing perovskite materials which have a ten times longer electron–hole diffusion length. The double fullerene layer structure is expected to find its broad application in many other perovskite devices with its excellent passivation effect.

Acknowledgements

The authors thank the financial support by the National Science Foundation under Awards ECCS-1201384 and ECCS-1252623 and the Nebraska Public Power District through the Nebraska Center for Energy Sciences Research.

References

1 Y. B. Yuan, T. J. Reece, P. Sharma, S. Poddar, S. Ducharme, A. Gruverman, Y. Yang and J. S. Huang, *Nat. Mater.*, 2011, **3**, 296–302.
2 I. Chung, B. Lee, J. He, R. P. H. Chang and M. G. Kanatzidis, *Nature*, 2012, **485**, 486–490.
3 G. Li, R. Zhu and Y. Yang, *Nat. Photonics*, 2012, **6**, 153–161.
4 G. Hodes, *Science*, 2013, **342**, 317–318.
5 Y. M. Sun, G. C. Welch, W. L. Leong, C. J. Takacs, G. C. Bazan and A. J. Heeger, *Nat. Mater.*, 2012, **11**, 44–48.
6 A. H. Ip, S. M. Thon, S. Hoogland, O. Voznyy, D. Zhitomirsky, R. Debnath, L. Levina, L. R. Rollny, G. H. Carey, A. Fischer, K. W. Kemp, I. J. Kramer, Z. Ning, A. J. Labelle, K. W. Chou, A. Amassian and E. H. Sargent, *Nat. Nanotechnol.*, 2012, **7**, 577–582.
7 S. H. Park, A. Roy, S. Beaupre, S. Cho, N. Coates, J. S. Moon, D. Moses, M. Leclerc, K. Lee and A. J. Heeger, *Nat. Photonics*, 2009, **3**, 297–303.
8 M. M. Lee, J. Teuscher, T. Miyasaka, T. N. Murakami and H. J. Snaith, *Science*, 2012, **338**, 643–647.
9 J. Burschka, N. Pellet, S. J. Moon, R. H. Baker, P. Gao, M. K. Nazeeruddin and M. Gratzel, *Nature*, 2013, **499**, 316–320.
10 M. Z. Liu, M. B. Johnston and H. J. Snaith, *Nature*, 2013, **501**, 395–398.
11 S. D. Stranks, G. E. Eperon, G. Grancini, C. Menelaou, M. J. P. Alcocer, T. Leijtens, L. M. Herz, A. Petrozza and H. J. Snaith, *Science*, 2013, **342**, 341–344.
12 H. J. Snaith, *J. Phys. Chem. Lett.*, 2013, **4**, 3623–3630.
13 A. Kojima, K. Teshima, Y. Shirai and T. Miyasaka, *J. Am. Chem. Soc.*, 2009, **131**, 6050–6051.
14 J. Y. Jeng, Y. F. Chiang, M. H. Lee, S. R. Peng, T. F. Guo, P. Chen and T. C. Wen, *Adv. Mater.*, 2013, **25**, 3727–3732.
15 G. C. Xing, N. Mathews, S. Y. Sun, S. S. Lim, Y. M. Lam, M. Gratzel, S. Mhaisalkar and T. C. Sum, *Science*, 2013, **342**, 344–347.
16 J. H. Im, C. R. Lee, J. W. Lee, S. W. Park and N. G. Park, *Nanoscale*, 2011, **3**, 4088–4093.
17 A. Abrusci, S. D. Stranks, P. Docampo, H. L. Yip, A. K. Y. Jen and H. J. Snaith, *Nano Lett.*, 2013, **13**, 3124–3128.
18 M. J. Carnie, C. Charbonneau, M. L. Davies, J. Troughton, T. M. Watson, K. Wojciechowski, H. Snaith and D. A. Worsley, *Chem. Commun.*, 2013, **49**, 7893–7895.
19 H. S. Kim, I. M. Sero, V. G. Pedro, F. F. Santiago, E. J. J. Perez, N. G. Park and J. Bisquert, *Nat. Commun.*, 2013, **4**, 2242.
20 N. G. Park, *J. Phys. Chem. Lett.*, 2013, **4**, 2423–2429.
21 W. Zhang, M. Saliba, S. D. Stranks, Y. Sun, X. Shi, U. Wiesner and H. J. Snaith, *Nano Lett.*, 2013, **13**, 4505–4510.
22 T. Baikie, Y. Fang, J. M. Kadro, M. Schreyer, F. Wei, S. G. Mhaisalkar, M. Graetzeld and T. J. White, *J. Mater. Chem. A*, 2013, **1**, 5628–5641.

23 V. I. Adamovich, S. R. Cordero, P. I. Djurovich, A. Tamayo, M. E. Thompson, B. W. DAndrade and S. R. Forrest, *Org. Electron.*, 2003, **4**, 77–87.
24 P. Peumans and S. R. Forrest, *Appl. Phys. Lett.*, 2001, **79**, 126–128.
25 P. Peumans, V. Bulovic and S. R. Forrest, *Appl. Phys. Lett.*, 2000, **76**, 2650–2652.
26 F. W. Guo, B. Yang, Y. B. Yuan, Z. G. Xiao, Q. F. Dong, Y. Bi and J. S. Huang, *Nat. Nanotechnol.*, 2012, **7**, 798–802.
27 F. W. Guo, Z. G. Xiao and J. Huang, *Adv. Optical Mater.*, 2013, **1**, 289–294.
28 P. Peumans, A. Yakimov and S. R. Forrest, *J. Appl. Phys.*, 2003, **93**, 3693–3723.
29 B. Yang, F. W. Guo, Y. B. Yuan, Z. G. Xiao, Y. Z. Lu, Q. F. Dong and J. S. Huang, *Adv. Mater.*, 2013, **25**, 572–577.
30 T. Walter, R. Herberholz, C. Muller and H. W. Schock, *J. Appl. Phys.*, 1996, **80**, 4411–4420.
31 U. Rau, D. A. Ras and T. Kirchartz, *Advanced characterization techniques for thin film solar cells*, John Wiley & Sons, 2011.
32 S. Khelifi, K. Decock, J. Lauwaert, H. Vrielinck, D. Spoltore, F. Piersimoni, J. Manca, A. Belghachi and M. Burgelman, *J. Appl. Phys.*, 2011, **110**, 094509.